ACS OMEGA

Article

Cite This: ACS Omega 2018, 3, 961−972

pH-Responsive Charge-Conversional and Hemolytic Activities of Magnetic Nanocomposite Particles for Cell-Targeted Hyperthermia

Md. Abdur Rahman,[†] Yoshimasa Matsumura,[†] Shigekazu Yano,[‡] and Bungo Ochiai*[,†]

[†]Department of Chemistry and Chemical Engineering, Graduate School of Science and Engineering and [‡]Department of Biochemical Engineering, Graduate School of Science and Engineering, Yamagata University, 4-3-16, Jonan, Yonezawa, Yamagata 992-8510, Japan

Supporting Information

ABSTRACT: Magnetic nanocomposite particle (MNP)-induced hyperthermia therapy has been restricted by inefficient cellular targeting. pH-responsive charge-conversional MNPs can enhance selective cellular uptake in acidic cells like tumors by sensing extracellular acidity based on their charge alteration. We have synthesized new, pH-induced charge-conversional, superparamagnetic, and single-cored Fe_3O_4 nanocomposite particles coated by *N*-itaconylated chitosan (NICS) cross-linked with ethylene glycol diglycidyl ether (EGDE) (Fe_3O_4-NICS-EGDE) using a simple, one-step chemical coprecipitation−coating process. The surface of the Fe_3O_4-NICS-EGDE nanocomposite particles was modified with ethanolamine (EA) via aza-Michael addition to enhance their buffering capacity, aqueous stability, and pH sensitivity. The designed Fe_3O_4-NICS-EGDE-EA nanocomposite particles showed pH-dependent charge-conversional properties, colloidal stability, and excellent hemocompatibility in physiological media. By contrast, the charge-conversional properties enabled microwave-induced hemolysis only under weakly acidic conditions. Therefore, the composite particles are highly feasible for magnetically induced and targeted cellular thermotherapeutic applications.

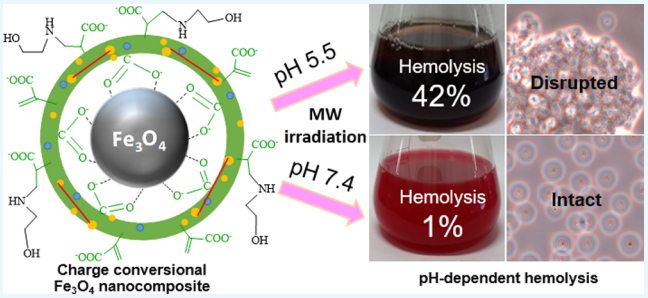

1. INTRODUCTION

Magnetic nanocomposite particles (MNPs) have been an attractive subject in nanotechnology and biomedicine because of their unique and promising properties. More specifically, iron oxide (Fe_3O_4 and Fe_2O_3) nanocomposite particles have been applied extensively in biomedical applications, such as diagnostic contrast agents for magnetic resonance imaging (MRI),[1−8] positron emission tomography,[3] single-photon emission computed tomography,[4] drug and gene delivery,[9−29] blood detoxification,[30] and magnetic hyperthermia therapy for tumors.[18,24−26,31−43] Most antitumor drugs still present many limitations, including poor solubility, short circulation kinetics, insufficient selectivity between malignant and healthy cells, and decreasing immune responses, causing adverse side effects.[11] MNPs may offer a solution by enhancing selectivity toward target cells. Tumor cells are more vulnerable to elevated temperature because of their holey vasculature, excessive cell proliferative hypoxia, and higher lymphatic drainage compared to normal tissues.[42] Therefore, killing cancer cells by hyperthermia method is an efficient method, as it is considered as a stand-alone and minimally invasive approach for tumor ablation.[33] Magnetic hyperthermia has already been proved for therapeutic efficacy in clinical trials.[40,41] It can indirectly boost the native antitumor immune responses[34] and also enhance the efficacy of other treatment methods, such as chemo- and radiation therapies.[31,32] In conventional magnetic hyperthermia, magnetic nanomaterials, such as iron oxide nanocomposites, are exposed to electromagnetic radiation sources, such as microwave (MW), or an alternating magnetic field (AMF) to generate heat. Heat is evolved through three mechanisms, hysteresis loss, Brownian relaxation, and Néel relaxation, depending on the size and concentration of the composites, heat capacity of the dispersion medium, and the frequency of the applied radiation.[33] The produced heat is transferred very quickly to the adjacent materials, but stays locally due to the low heat-transfer capacity of physiological fluids, such as blood, lymph, and intracellular fluids, resulting in highly focused heating.[35,36] However, unspecific and inadequate delivery of MNPs induces severe side effects, sublethal temperature changes, resistance in malignant cells, and damage to healthy cells.[37]

To address these issues, various methodologies have been developed.[7] Recently, it has been reported that targeted MNPs can generate ultrasound waves by their mechanical oscillation in a nonhomogeneous AMF.[36,43,44] The generated intracellular ultrasound can lyse malignant cells like magnetic hyperthermia, without showing any increment in surrounding temperature. The external surface of MNPs is often engineered with various tissue-interactive substances, such as peptides,[45,46] small molecules,[21] antibodies,[6] nucleic acid aptamers,[5,10,38] carbohydrates,[2] and nonimmunoglobulin scaffolds.[7] These ligands can improve the interaction between the nanocomposite particles

Received: December 4, 2017
Accepted: January 16, 2018
Published: January 25, 2018

DOI: 10.1021/acsomega.7b01918
ACS Omega 2018, 3, 961−972

Scheme 1. Synthesis of NICS via Amidation of CS with IAn

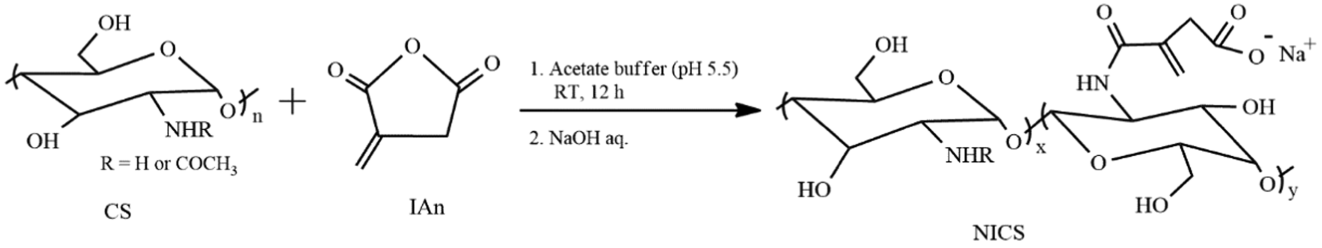

and target cells. In another approach, PEGylated magnetic liposomes[39] were fabricated by conjugating poly(ethylene glycol) (PEG) to the liposome surface, reported to enhance the accumulation of liposomes in tumor cells through the enhanced permeation and retention effect facilitated by their long circulation time.[13,47] However, the excessively hydrated shell of PEGylated liposomes causes a severe problem associated with their limited cellular uptake in targeted areas, resulting in nonselective cell heating.[14,16] Strategies to improve targeting ability have introduced stimuli-responsive (temperature, light, sound, pH, etc.) properties to magnetic materials.[16−20,24−26] Among them, pH-sensitive magnetic particles are advantageous in facileness and targeting ability to malignant sites in acidic environments, potentially minimizing adverse side effects associated with nontargeted areas.[27] Tumors are one of the most focused targets for pH-responsive nanoparticles[16,19,22,23] because tumor tissues (pH 5.7−7.2) and their intracellular compartments, such as endosomes (pH 5.0−6.5) and lysosomes (pH 4.5−5.0), are more acidic in nature than the blood stream and healthy cells (pH 7.4).[27] The pH responsiveness of MNPs with charge-conversional ability may solve the problem of traditional magnetic particles applied for hyperthermia, whereby their concentration typically decreases very rapidly during circulation because of the systemic clearance or uncontrolled transportation before reaching the tumor cells.

pH-induced charge-conversional Fe_3O_4 nanoparticles with cross-linked shells were reported for hyperthermia and chemotherapy.[26] Under acidic conditions, the negatively charged nanocarriers were converted into positively charged ones and released electrostatically bound drugs. The drug release was enhanced by AMF for efficient cytotoxicity to tumor cells. Charge reversal magnetic MNPs based on electrostatic interaction was also reported for pH-sensitive drug delivery.[27] Cationically modified Fe_3O_4 nanoparticles were electrostatically complexed with carboxylated dextran (Dex-COOH) to generate negatively charged surfaces and electrostatically incorporated the drug molecules. The electrostatic linkage was broken under low pH, and both Dex-COOH and loaded drug were released in the nuclei of HeLa cells. High antitumor activity with an IC_{50} of 0.7 μg mL^{-1} was attained. These studies validated that pH-induced charge-conversional MNPs could be applied for tumor cell-targeted therapies. pH-responsive MNPs were fabricated using various strategies,[21−29] but facile approaches without the use of any surfactants and organic solvents are highly desirable for biomedical applications. Accordingly, we focused on a one-step chemical coprecipitation−coating method, in which magnetic cores were synthesized by coprecipitation of their corresponding saturated salt solution in aqueous basic medium and the produced core-particle surface was concomitantly passivated with pH-sensitive polymeric stabilizers. Among pH-sensitive artificial and natural polymers, chitosan (CS) and its derivatives have been used to functionalize MNPs because of their excellent biorelated properties.[8,21,23,29] For example, CS-functionalized mesoporous MNPs were reported for pH-responsive controlled release of an antineoplastic drug.[29] CS was employed for enhancing their biocompatibility and electrostatic loading capacity of the drug molecules. The loaded drug was released by releasing CS under acidic pH. However, the synthetic procedures of the composite required multiple steps, including uses of organic solvents and surfactants. *N*-Naphthyl-*O*-dimethylmaleoyl CS-based therapeutic MNPs were designed for pH-sensitive drug delivery and imaging for cancer.[8] This material successfully targeted tumors in vivo and was applied as an MRI contrast agent, thereby requiring a multistep synthetic technique. Hybrid MNPs coated with maltose-modified CS (CS-Malt) were also reported for antitumor drug delivery.[21] Fe_3O_4 particles were prepared by coprecipitation and coated with CS-Malt, followed by both ionic and covalent cross-linkage with Na_2SO_4 and glutaraldehyde, respectively, in reverse emulsion.

However, employing organic solvents and surfactants in the fabrication of some MNPs requires their careful and tedious removal for subsequent biorelated applications. In addition, noncovalent coating of MNPs involves problems associated with serum interaction and destabilization during circulation. Therefore, pH-responsive charge-conversional MNPs require further design, namely, nanosized and single-cored features, covalent fixing, and charge conversion by pH trigger with colloidal stability at physiological pH, and selective accumulation in acidic environments.

In this study, we report the fabrication and characterization of pH-responsive charge-conversional MNPs designed for cell-targeted therapeutic applications. We employed *N*-itaconylated CS (NICS) modified by ethanolamine (EA) for a charge-conversional and biocompatible scaffold prepared by a very simple procedure. The MNPs are composed of a single Fe_3O_4 core and covalently cross-linked NICS polymeric coating, synthesized by a facile one-step chemical coprecipitation−coating method, followed by EA functionalization. We confirmed their structure, pH-dependent size, surface properties, physiological stability, hemolytic behavior, and magnetic response. We finally tested them for their feasibility in targeted hyperthermia therapy. The magnetic and pH-responsive properties of these composite particles would offer spatial and temporal control for selective targeting of acidic cells.

2. RESULTS AND DISCUSSION

2.1. Synthesis and Characterization of NICS. NICS was synthesized by partial modification of the amino groups of CS with itaconic anhydride (IAn) to achieve controllable aqueous solubility and desired reactivity for further modification. The modification proceeded through the half amidation of the anhydride moieties of IAn, and the resulting carboxy group was

DOI: 10.1021/acsomega.7b01918
ACS Omega 2018, 3, 961−972

Scheme 2. Fabrication of Fe_3O_4-NICS-EGDE-EA Nanocomposite Particles by a Simple Coprecipitation−Coating Method, Followed by Aqueous Aza-Michael Addition of EA

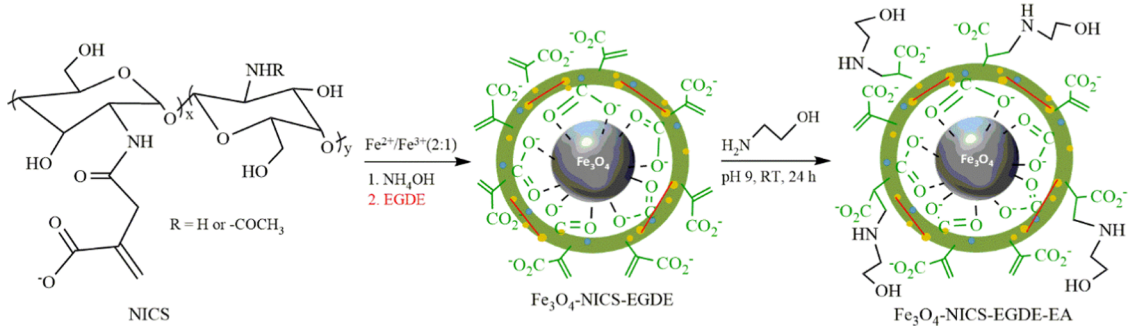

readily converted into a mono-Na-itaconate by neutralizing with NaOH aq. (Scheme 1). The resulting compound was characterized by ^{1}H nuclear magnetic resonance (NMR), Fourier transform infrared (FTIR) spectroscopy, and X-ray diffraction (XRD, Figure S1). The ^{1}H NMR spectroscopic data revealed that 36% of the amine moieties of the CS chain were substituted by *N*-itaconyl moieties (Figure S1a). The FTIR spectrum of NICS showed the successful incorporation of the *N*-itaconyl moieties to the nitrogen of the D-glucosamine unit of CS (Figure S1b). XRD analysis (Figure S1c) demonstrated the effect of introducing hydrophilic groups to the CS backbone. The resulting NICS exhibited semicrystalline microstructure with appreciable water solubility in a manner similar to that reported for *N*-succinyl CS.[48]

2.2. Synthesis and Functionalization of Fe_3O_4-NICS-EGDE Nanocomposite Particles. NICS was applied as a template and surface modifier for Fe_3O_4 through a simple two-step process. The first step involves the fabrication of nanocomposite particles of Fe_3O_4 and concomitant coating by NICS, followed by cross-linking with ethylene glycol diglycidyl ether (EGDE) (Fe_3O_4-NICS-EGDE) via a facile chemical coprecipitation−coating technique (Scheme 2). In this process, Fe_3O_4 was formed in a basic aqueous solution of $FeSO_4$ and $FeCl_3$ containing NICS via coprecipitation of Fe^{2+} and Fe^{3+} ions and simultaneously coated by chelation of the carboxylate moieties of NICS on the surface of Fe_3O_4 nanocrystals. Coated NICS was subsequently cross-linked via the ring-opening addition of the amine moieties of NICS to the epoxy ring of EGDE to restrict probable escaping of Fe_3O_4 particles during circulation. The resulted Fe_3O_4-NICS-EGDE nanocomposite particles are unable to form highly stable dispersion in physiological buffers because of the zwitterionic character of NICS, which contains both the amine and carboxy moieties. The presence of alkenyl, carboxy, hydroxy, and amine functions in a single Fe_3O_4-NICS-EGDE nanocomposite particle allows its easy modification by conjugation to sensitive moieties. Specifically, the electron-deficient alkenyl group is a highly reactive site for aza-Michael addition reaction in aqueous media. In the second step, the Fe_3O_4-NICS-EGDE nanocomposite particles were modified via the aqueous aza-Michael addition of EA to the alkenyl groups to achieve better colloidal stability and improved pH responsiveness (Scheme 2).

2.3. Structure of Nanocomposites. The successful fabrication of the Fe_3O_4-NICS-EGDE and Fe_3O_4-NICS-EGDE-EA nanocomposite particles was confirmed by FTIR spectroscopy (Figure 1), energy-dispersive X-ray (EDX) spectrometry (Figure S3), XRD (Figure S4), high-resolution transmission electron microscopy, selected area electron

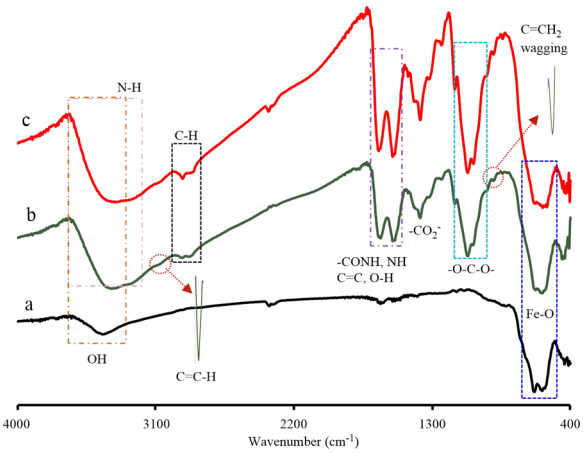

Figure 1. FTIR spectra of (a) bare Fe_3O_4, (b) Fe_3O_4-NICS-EGDE, and (c) Fe_3O_4-NICS-EGDE-EA nanocomposite particles.

diffraction (Figure S5), and ^{1}H NMR analysis of a model polymer. The FTIR spectrum of bare Fe_3O_4 (Figure 1a) shows two strong absorption bands at 584 and 632 cm^{-1} assignable to the stretching of the Fe−O bond in the crystalline lattice of Fe_3O_4, which were also observed in the spectra of both composites. A broad signal appearing at 3435 cm^{-1} is assignable to the absorption of hydrogen-bonded O−H, indicating the fabrication of Fe_3O_4 in aqueous environment.[49−51] In the FTIR spectrum of Fe_3O_4-NICS-EGDE prepared in situ (Figure 1b), the carbonyl stretching absorption of carboxylate moieties originating from NICS significantly shifted from 1382 to 1375 cm^{-1}, indicating the coordination of $-CO_2^-$ ions to Fe_3O_4.[52] In addition, two new signals with very weak intensities (shown in enlarged formats) appearing at 3073 and 893 cm^{-1} are assignable to the stretching of alkenyl C−H and the wagging of C=CH_2, respectively.[53] Two medium-intense bands were also observed at 1555 and 1634 cm^{-1}, which are assignable to the absorption of amides I and II and C=C, respectively.[54] A very broad signal observed in the region of 3330−3440 cm^{-1} is assignable to the stretching vibration bands of O−H and N−H groups, respectively. These results indicate that the surface of Fe_3O_4 was efficiently coated with NICS-EGDE. In the spectrum of the Fe_3O_4-NICS-EGDE-EA nanocomposite (Figure 1c), the amide I and II peaks appeared at higher wavenumbers (1557 and 1646 cm^{-1}, respectively) than those in the spectrum of Fe_3O_4-NICS-EGDE, indicating that the α,β-unsaturated amine moieties were transformed into saturated structures. In addition, the intensity of the C−N and C−H stretching bands became stronger. These results demonstrate

DOI: 10.1021/acsomega.7b01918
ACS Omega 2018, 3, 961−972

Scheme 3. Model Reaction between NICS and EA

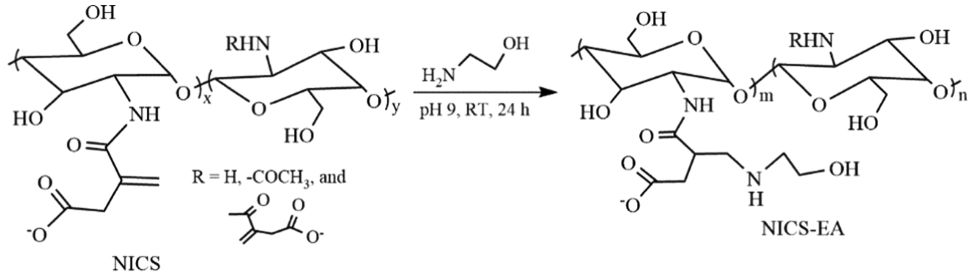

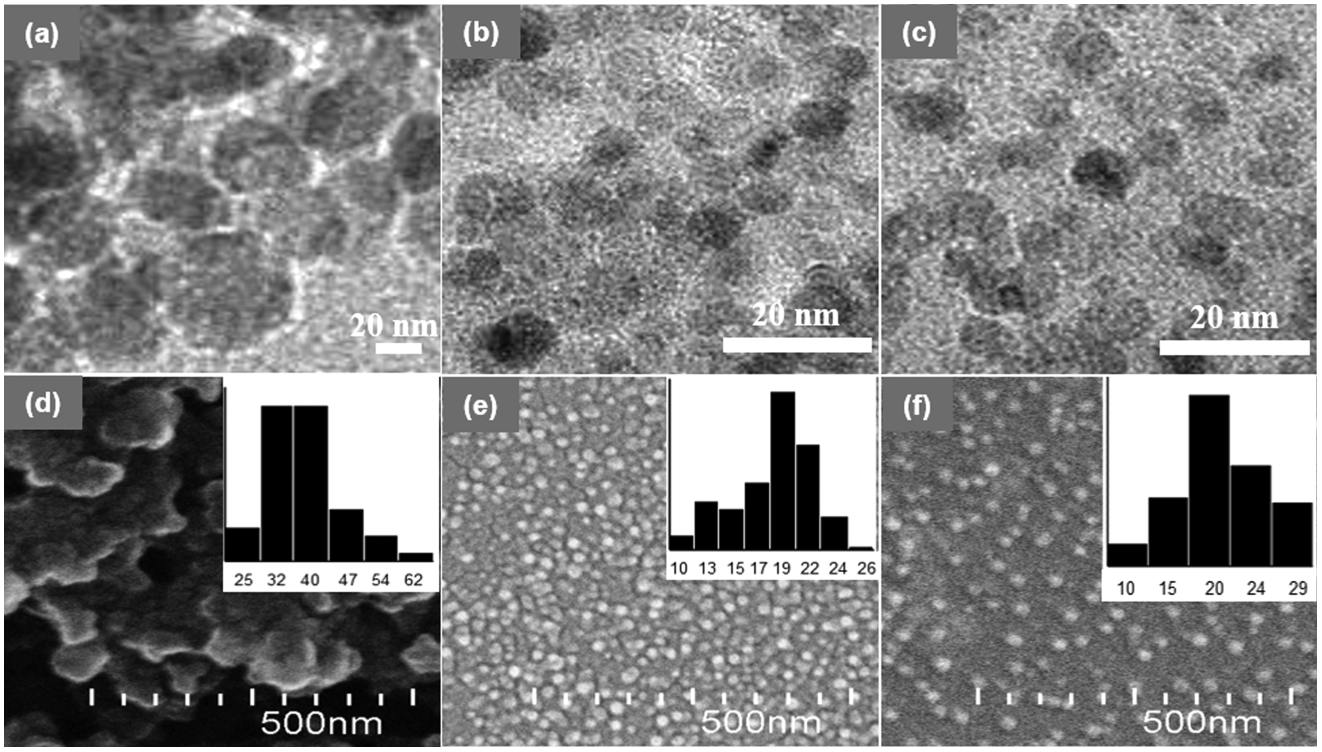

Figure 2. TEM images (a–c) and SEM images (d–f) of bare Fe_3O_4, Fe_3O_4-NICS-EGDE, and Fe_3O_4-NICS-EGDE-EA nanocomposite particles.

the addition of EA to the alkenyl moieties of Fe_3O_4-NICS-EGDE.

The progress of EA addition to NICS was further confirmed by a model reaction of NICS and EA under identical conditions because the cross-linkage and the paramagnetic character prevented the quantitative analysis (Scheme 3). The ^{1}H NMR spectrum of NICS-EA shows three characteristic peaks at 2.9, 3.4, and 3.6 ppm (Figure S2). These signals are assignable to the $-CH_2NCH_2-$ and $-OCH_2-$ protons originating from the aza-Michael addition of EA to the pendant *N*-itaconyl moieties. The alkenyl protons were also observed at 5.35 and 5.75 ppm, indicating the partial addition of EA to NICS. The percentage of EA addition was calculated to be 27% from the integral ratio of the ^{1}H NMR peaks of the $-NCH_2CH_2OH$ and acetyl protons in NICS-EA.

2.4. Morphology of Nanocomposites. The bare Fe_3O_4, Fe_3O_4-NICS-EGDE, and Fe_3O_4-NICS-EGDE-EA nanocomposite particles were analyzed by transmission electron microscopy (TEM, Figure 2a–c). The TEM image of bare Fe_3O_4 shows spherical particles with an average diameter of 40 nm. As the bare Fe_3O_4 particles were prepared in the absence of any stabilizers, the growth of particle was higher, resulting in aggregation compared to the in situ prepared Fe_3O_4 nanocomposite particles. Therefore, the TEM images of both composites showed similar shapes with average diameters of 7 nm regardless of the sample due to the control growth of particles in solution. This result indicates that the core was not deteriorated during the coating and functionalization process. The surface morphologies and particle sizes of the dried Fe_3O_4, Fe_3O_4-NICS-EGDE, and Fe_3O_4-NICS-EGDE-EA nanocomposite particles were also studied by scanning electron microscopy (SEM, Figure 2d–f). The histograms shown in the insets indicate their size distributions. The bare Fe_3O_4 particles were observed as aggregates due to the absence of any stabilizer. The average size was approximately 40 nm, but the aggregation resulted in difficulty in size calculation, and probably resulted in overestimation. The Fe_3O_4-NICS-EGDE nanocomposite particles prepared in situ showed spherical shapes with an average diameter of 21 nm and exhibited good colloidal dispersity compared to bare Fe_3O_4 particles. The Fe_3O_4-NICS-EGDE-EA nanocomposite particles were also spherical in shape with an average diameter of 22 nm, and the colloidal dispersity was better than that of the unmodified composites. The relatively larger sizes than the TEM images originated from the coating layers of the composites without having heavier atoms that were not observed in the TEM images.[2,52,54] The spherical

DOI: 10.1021/acsomega.7b01918
ACS Omega 2018, 3, 961–972

morphology and the smaller size indicate that each nanocomposite particle mostly contains a single Fe_3O_4 core. The quantities of the organic coatings of the Fe_3O_4-NICS-EGDE and Fe_3O_4-NICS-EGDE-EA nanocomposite particles were estimated to be 27 and 28%, respectively, by thermogravimetric analysis (TGA, Figure S6).

2.5. Magnetism of Nanocomposites. The magnetic properties of the dried, bare Fe_3O_4, Fe_3O_4-NICS-EGDE, and Fe_3O_4-NICS-EGDE-EA nanocomposites were investigated by measuring their magnetization as a function of the applied magnetic field at ambient temperature (Figure 3). The magnetization profiles for all samples exhibited the existence of open hysteresis loops in their $M-H$ curves with negligible remanence and coercivity, suggesting that these materials are composed of a single-domain particle with superparamagnetic properties like typical Fe_3O_4.[50,55] The saturation magnetization (M_s) was calculated with respect to the mass of Fe_3O_4. The M_s values of Fe_3O_4 cores inside Fe_3O_4-NICS-EGDE and Fe_3O_4-NICS-EGDE-EA nanocomposite particles were 80 and 78 emu g^{-1}, respectively. These values are higher than the M_s value of the bare Fe_3O_4 particles (70 emu g^{-1}). The increment in M_s of the nanocomposites plausibly originated from the improvements in the uniformity in the surface properties of the Fe_3O_4 coated in situ via chemical bonding to the carboxylate moieties of NICS, as reported for the alginic acid-coated Fe_3O_4 nanoparticles.[56] The high M_s value of the Fe_3O_4-NICS-EGDE-EA nanocomposite particles will be advantageous for magnetic guiding applications, such as hyperthermia therapy for cancer cells, because of the rapid response to external magnetic fields.

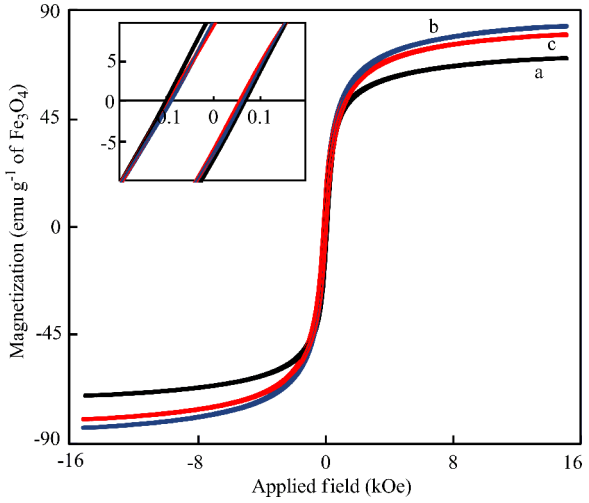

Figure 3. Magnetic hysteresis curves of dried (a) bare Fe_3O_4, (b) Fe_3O_4-NICS-EGDE, and (c) Fe_3O_4-NICS-EGDE-EA nanocomposite particles analyzed by vibrating sample magnetometry at room temperature. The inset indicates a region of lower magnetic field.

2.6. Effect of pH on Size, ζ Potential, and Colloidal Stability of Nanocomposites. The average hydrodynamic size, ζ potential, and colloidal stability of the nanocomposites were studied by dynamic light scattering (DLS) in Dulbecco's phosphate-buffered saline (DPBS) with controlled pH from 3 to 9 (as prepared, Figure 4a–c). The average hydrodynamic diameters were almost identical (ca. 300 nm) in the pH range of 3–5, and the particles were highly dispersible. However, the average hydrodynamic size of the Fe_3O_4-NICS-EGDE-EA nanocomposite was increased significantly at pH 5.5–6.0, resulting in gradual accumulation of the nanocomposite particles (Figure 4d). Above pH 6, the nanocomposites again became highly dispersible. These pH-dependent variations in size and dispersibility originated from the charge-conversional functions of the nanocomposites that consisted of carboxyl and

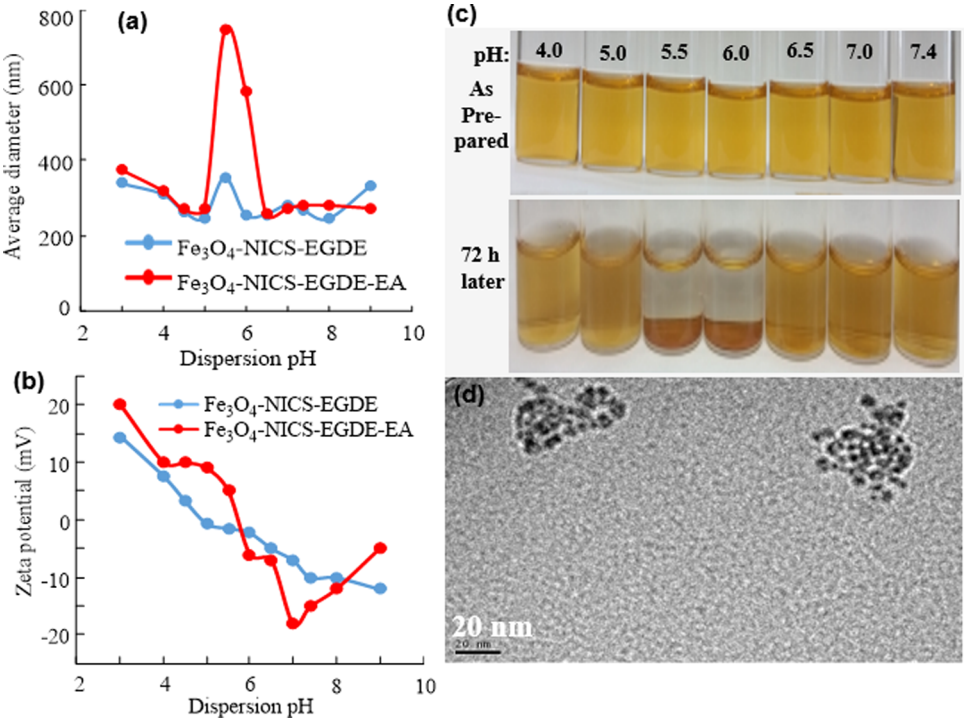

Figure 4. pH-dependent (a) hydrodynamic diameter, (b) ζ potential, (c, d) aqueous stability, and (e) TEM image of Fe_3O_4-NICS-EGDE-EA nanocomposite particles cast from pH 5.5 dispersion.

DOI: 10.1021/acsomega.7b01918
ACS Omega 2018, 3, 961–972

amine moieties. The net electrostatic repulsions among the individual composite particles are sufficient when they are either cationically or anionically charged. The positive ζ potentials at pH 3−5 indicate the predominant protonation of the amine and carboxylate groups of the composites. In a similar manner, the negative ζ potentials above pH 6 indicate the predominant deprotonation of the ammonium and carboxy groups. By contrast, the composites became almost charge-neutral in the pH range of unstable dispersion. Under these conditions, the zwitterionic surface of the nanocomposites were ionically cross-linked, leading to gradual aggregation. This behavior is much stronger for the Fe_3O_4-NICS-EGDE-EA nanocomposite than for the unmodified Fe_3O_4-NICS-EGDE nanocomposite. The aggregation tendency was further confirmed by the assembled mass in the TEM image of the Fe_3O_4-NICS-EGDE-EA cast from dispersion at pH 5.5 (Figure 4e), contrastive to the SEM image indicating the dispersed particles (Figure 2f).

The Fe_3O_4-NICS-EGDE-EA nanocomposite particles were highly dispersible at physiological pH because of the mild negative surface charge (−15 mV). The conversion into isoelectric charge under weakly acidic conditions enabled the Fe_3O_4-NICS-EGDE-EA nanocomposite to act as a smart magnetic switch suitable for the magnetothermal treatment of acidic cells.

2.7. Buffering Capacity of Nanocomposites. The relative buffering abilities of the Fe_3O_4-NICS-EGDE and Fe_3O_4-NICS-EGDE-EA nanocomposite particles were studied using acid−base titration to evaluate buffering capacity affecting the proton-sponge effect in endosomal escape and cytosolic delivery (Figure 5).[27,28] The charge-conversional Fe_3O_4-NICS-EGDE-EA nanocomposite particles exhibited stronger buffering effect in the pH range of 5.0−7.5 than did Fe_3O_4-NICS-EGDE, which can be ascribed to the presence of a substantial number of secondary amine groups originating from EA in addition to the $-COO^-$ and the primary amine moieties inherently included in CS. The high buffering capability of the charge-conversional nanocomposite particles is advantageous for protonation in endosomes with relatively weaker pH, resulting in endosomal membrane disruption and endosomal escape of the system.

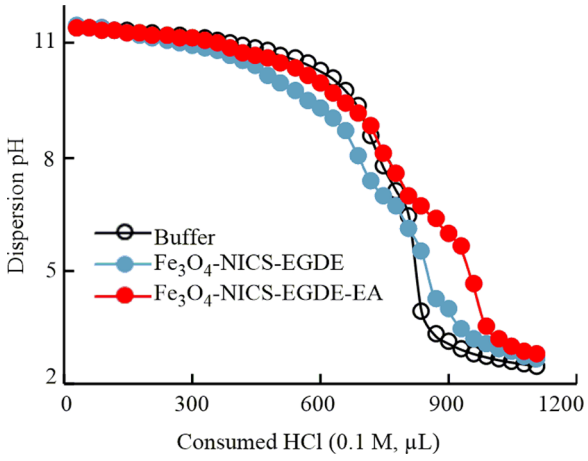

Figure 5. Buffer capacity of Fe_3O_4-NICS-EGDE and Fe_3O_4-NICS-EGDE-EA nanocomposite particles (1 mg mL^{-1}) in 150 mM NaCl aq. buffer (initial pH 11.50) titrated with 0.1 M HCl aq.

2.8. pH-Dependent Hemolysis of RBCs by Fe_3O_4-NICS-EGDE-EA Nanocomposite Particles. The hemocompatibility of theranostic nanoparticles is essential for their systemic internalization. Accordingly, we examined the impact of charge-conversional Fe_3O_4-NICS-EGDE-EA nanocomposite particles on sheep red blood cells (RBCs) using a hemolysis assay at 37 °C for 5 h. Figure 6 depicts the pH-dependent hemolytic activities of the charge-conversional Fe_3O_4-NICS-EGDE-EA nanocomposite particles. The degree of hemolysis increased with increasing nanocomposite concentration and decreasing pH, but it remained below 2%. This enhancement of hemolysis in low-pH media originated from the decrease in the surface anionic characteristic of the nanocomposite particles, which strengthens interactions between the nanocomposite particles, and the negative surface of RBC membranes, resulting in hemolytic potential that is 3 times higher at pH 5.0 than that at pH 7.4. The nanocomposite particles showed negligible hemolytic activity at pH 7.4, and it was only 0.59% even at very high concentration (600 μg mL^{-1}) because of their mildly negative surface charge. The degree of hemolysis was increased with increasing incubation periods (Figure S7), but it remained below 1.0% under physiological conditions after 5 h. These values are still approximately 10 times lower than the permissible limit of hemolysis for blood-contacting biomaterials.[57] Although the charge-conversional Fe_3O_4-NICS-EGDE-EA nanocomposite particles were sufficiently dispersed in the RBC suspension under the examined conditions, the unmodified Fe_3O_4-NICS-EGDE nanocomposite particles were not dispersible under the physiological conditions (Figure S8a−c). As a result, the hemolytic activities of the unmodified Fe_3O_4-NICS-EGDE nanocomposite particles were negligible (below 0.5%, Figure S8d) because of the negligible interaction, but the insufficient dispersibility prevents their practical applications. Furthermore, the hemolytic activity of the charge-conversional Fe_3O_4-NICS-EGDE-EA nanocomposite particles is lower than that previously reported for CS-coated Fe_3O_4 materials. For example, the degree of hemolysis of sheep RBCs was 3.2% in our previously reported Fe_3O_4 coated with carboxy-functionalized CS at 500 μg mL^{-1}.[54] In another report,[20] Fe_3O_4 coated with CS-Malt designed for drug delivery showed 4.9% hemolysis toward human RBCs at 400 μg mL^{-1}. The higher

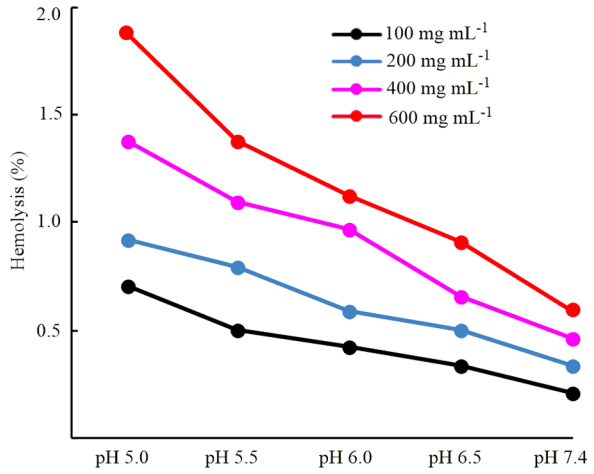

Figure 6. Hemolytic activities of charge-conversional Fe_3O_4-NICS-EGDE-EA nanocomposite particles toward sheep RBCs in physiological solution (150 mM NaCl aq.) incubated at 37 °C for 5 h.

DOI: 10.1021/acsomega.7b01918
ACS Omega 2018, 3, 961−972

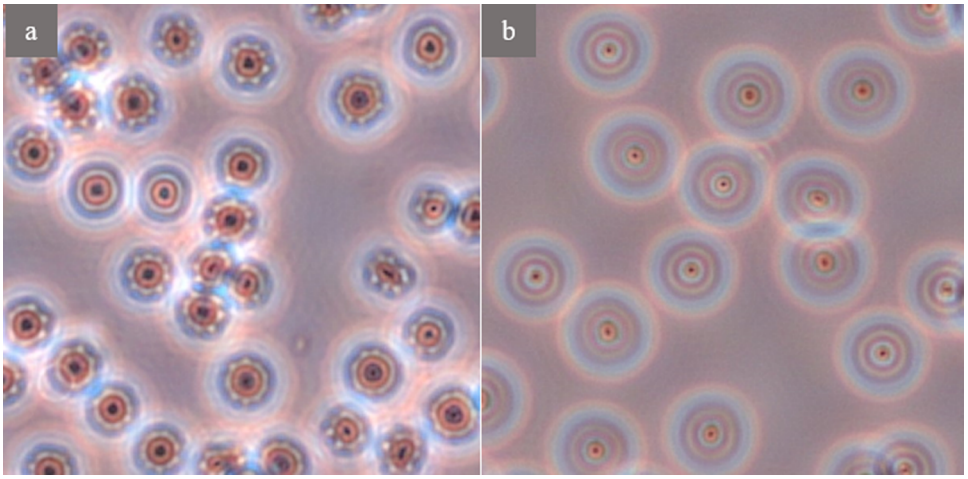

Figure 7. Light microscopic images of RBCs incubated at pH 5.5 for 5 h (a) with and (b) without (control) 600 μg mL^{-1} Fe_3O_4-NICS-EGDE-EA nanocomposite particles.

hemocompatibility of charge-conversional Fe_3O_4-NICS-EGDE-EA nanocomposite particles is ascribable to its charge (−15 mV), which is identical to that of healthy RBCs (−15.7 mV)[58] and milder than that of the aforementioned materials (−27 and −52 mV).

2.9. Morphology of RBCs. Figure 7 illustrates the morphologies of RBCs in the presence and absence of the charge-conversional Fe_3O_4-NICS-EGDE-EA nanocomposite particles incubated at pH 5.5 for 5 h. The nanocomposite particles were cationically charged at this pH by charge conversion via the protonation of the surface amine groups. As a result, the particles were adhered on the surface of RBC membranes and caused structural distortion and aggregation of RBCs (Figure 7a), whereas the RBCs maintained their native morphology in the absence of the nanocomposite particles (Figure 7b). Hemolysis proceeded during incubation as confirmed by optical microscopic studies (Figure S9). This pH-dependent interaction with RBC membranes implies the application of the charge-conversional Fe_3O_4-NICS-EGDE-EA nanocomposite particles in targeting acidic cells, such as inflamed and tumor cells.

2.10. Temperature Evolution under MW Irradiation. The energy dissipation and hemolytic abilities of the charge-conversional Fe_3O_4-NICS-EGDE-EA nanocomposite particles were evaluated under MW-induced magnetic heating (Figure 8). The heating experiments were conducted at physiological pH (7.4) and acidic pH (5.5), where the composite adhered to RBCs. Here, the RBC suspension was used as a model system for cell lines. The temperature rose as MW irradiation progressed in the identical tendency regardless of the sample, indicating the ignorable effect of the magnetic nanocomposite on the global temperature of the system. For example, the temperatures after 180 s MW irradiation was in the range of 50−54 °C. However, the color of the medium was changed significantly from red to black only in the sample with the nanocomposite particles at pH 5.5, as indicated in the inset image (Figure 8), demonstrating significant pH-dependent membranolysis of RBCs, as described later.

2.11. pH-Triggered, MW-Induced Membranolysis of RBCs by Fe_3O_4-NICS-EGDE-EA Nanocomposite. We presumed that the selective change in color originated from the synergistic effects of MW irradiation and the adherence of the charge-conversional Fe_3O_4-NICS-EGDE-EA nanocomposite particles. Accordingly, the hemolysis behavior under MW irradiation was investigated in detail. RBCs were incubated with different concentrations (25, 50, and 100 μg mL^{-1}) of the charge-conversional Fe_3O_4-NICS-EGDE-EA nanocomposite particles dispersed in 100 mL of buffer (150 mM NaCl aq.) at pHs 5.5, 6.5, 6.8, and 7.4. These slightly acidic conditions were selected for models of typical extracellular (pH = 6.5−7.0)[59−61] and intracellular (pH = 4.5−7.2)[25−27] environments of cancers. After incubation for 5 h at 37 °C, each sample and controls were exposed to MW for 30 s and their temperature was measured. The temperature of all samples and controls were within the range of 42−45 °C. Despite the identical temperature, significant discoloration of the RBC suspension from red to black occurred in the samples at pH 5.5, whereas partial discoloration (Figure S10a,b) were observed for the samples at pHs 6.8 and 6.5. The degree of hemolysis was increased with the increase of the concentration of the charge-conversional Fe_3O_4-NICS-EGDE-EA nanocomposite particles and the decrease of pH (Figure 9a). For example, the degrees of hemolysis by 100 μg mL^{-1} of the charge-conversional Fe_3O_4-

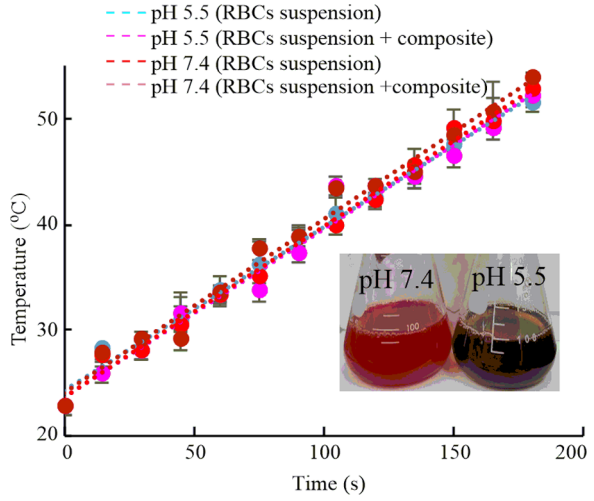

Figure 8. Temperature evolution of RBC suspension (150 mM NaCl aq.) in the presence and absence of Fe_3O_4-NICS-EGDE-EA nanocomposite particles under MW irradiation at pHs 7.4 and 5.5. Inset: RBC suspension after MW irradiation: composite concentration 100 μg mL^{-1}.

DOI: 10.1021/acsomega.7b01918
ACS Omega 2018, 3, 961−972

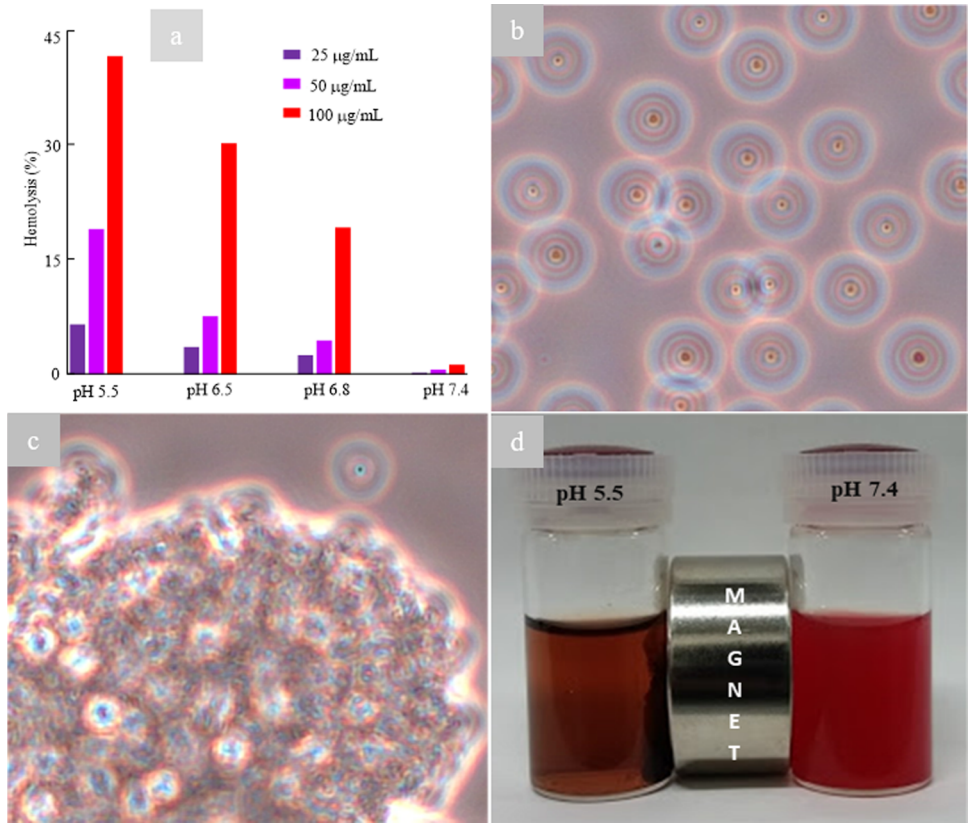

Figure 9. MW-induced disruption of RBC membrane (hemolysis) by charge-conversional Fe_3O_4-NICS-EGDE-EA nanocomposite particles (30 s of MW irradiation after incubation at 37 °C for 5 h, 100 μg mL^{-1} nanocomposite). (a) Effect of pH and concentration on hemolysis. Typical light microscopic images of MW-irradiated RBC suspension in 150 mM NaCl aq. buffer at (b) pH 7.4 and (c) pH 5.5. (d) Photo of magnetic separation.

NICS-EGDE-EA nanocomposite particles were 19, 30, and 42% at pHs 6.8, 6.5, and 5.5, respectively. On the other hand, at pH 7.4, the charge-conversional Fe_3O_4-NICS-EGDE-EA nanocomposite particles exhibited negligible hemolytic activities under the identical conditions, as explained earlier. To confirm these results, RBC dispersions containing 100 μg mL^{-1} nanocomposite particles were observed under an optical microscope. At pH 7.4, the RBCs maintained their regular shape without membrane destruction (Figure 9b), whereas they were mostly damaged at pH 5.5 (Figure 9c) and partially disrupted at pHs 6.8 and 6.5 (Figure S10c,d). This pH-dependent membranolysis of RBC can be explained by the difference in the adherence of the nanocomposite particles toward the membranes of RBC originating from the surface charge-conversional property described in Figure 4. The membrane rapture was further certified by magnetic separation of the broken RBC debris containing the MNPs in the dispersed medium, whereas the RBCs dispersed under identical condition at pH 7.4 were not attracted at all by a magnet (Figure 9d). This selective magnetic separation demonstrates the enhanced magnetism by particle accumulation, as well as the magnetic targetability and acidity-sensing ability of the charge-conversional Fe_3O_4-NICS-EGDE-EA nanocomposite particles. A similar behavior was reported for targeted iron oxide MNPs that could selectively reach to the tumor cells and cause their lysis by AMF-induced heating.[44,45] This difference clearly manifests that the Fe_3O_4-NICS-EGDE-EA nanocomposite particles only interacted with RBCs when they were cationically charged under acidic conditions, resulting in local hyperthermia or MW-induced particle rotation disrupting the membrane of RBCs.

3. CONCLUSIONS

A charge-conversional, magnetically targetable, and covalently cross-linked NICS-coated Fe_3O_4 nanocomposite was successfully synthesized. The nanocomposite particles were composed of highly crystalline, nanosized, superparamagnetic, and single Fe_3O_4 cores with a thin coated layer of functionalized polysaccharides. Significant pH responsiveness and colloidal stability in physiological buffers were introduced to the nanocomposite particles via surface modification with EA. In acidic environments, the charge-conversional nanocomposite particles converted the ζ potential from negative to positive, confirming the responsiveness to variable environments. The nanocomposite particles self-assembled specifically in weakly acidic environments to offer relatively stronger magnetism than under physiological conditions. The nanocomposite adhered to RBCs at a weakly acidic pH range, whereas they did not interact under physiological conditions. Because of this specific interaction, the MW-induced hemolysis of RBCs effectively occurred at pHs 5.5−6.8 with a change in global temperature identical to that in the absence of the nanocomposite or at physiological pH. As the conversion into cationic charge was attained under slightly acidic environments, the resultant positive surface charge is advantageous in the uptake processes of acidic cells proceeding through membrane adhesion and endocytosis. Although the present form of the composite showed excellent performance for membranolysis of RBC, optimization of the functionalization degrees and the functional

DOI: 10.1021/acsomega.7b01918
ACS Omega 2018, 3, 961−972

groups will further improve the selectivity and targeting ability toward acidic cells. For example, as the charge-conversional Fe_3O_4-NICS-EGDE-EA nanocomposite possesses alkenyl, carboxy, and amine groups, conjugation with bioactive agents, such as peptides, may synergistically improve the efficacy. We anticipate that our designed system will find practical applications in cell-specific thermotherapy for cancer.

4. EXPERIMENTAL SECTION

4.1. Materials. CS (M_w = 5.6 × 10^5 g mol^{-1}), EA, EGDE, and IAn were purchased from Tokyo Chemical Industry (Tokyo, Japan). $FeSO_4·7H_2O$ was purchased from Sigma-Aldrich (St. Louis, MO). Ammonia solution (28%) and $FeCl_3·6H_2O$ were purchased from Kanto Chemical (Tokyo, Japan). Preserved sheep whole blood was purchased from Cosmo Bio (Tokyo, Japan). Deionized distilled water (DDW) was used throughout the study. DPBS was purchased from Gibco Life Technologies (Piasley, U.K.). All other reagents used in this study were of lab grade and used without further purification.

4.2. Measurements. ^{1}H NMR spectra were recorded on a JEOL (Tokyo, Japan) ECX-400 instrument using tetramethylsilane as an internal standard (400 MHz). FTIR spectra were recorded on a JASCO (Tokyo, Japan) FTIR-460 plus spectrometer. Hydrodynamic diameter and ζ potential were analyzed using DLS on a Malvern Instruments (Malvern, U.K.) Zetasizer Nano ZS. EDX spectra were recorded on a JEOL (Tokyo, Japan) JSM-6510A analytical scanning electron microscope. SEM measurements were conducted on a Hitachi (Tokyo, Japan) SU8000 microscope at an accelerating voltage of 30 kV. TEM measurements were conducted on a JEOL (Tokyo, Japan) TEM-2100F field emission scanning electron microscope. The XRD patterns were measured on a Rigaku (Tokyo, Japan) Ultima IV RINT D/max-kA diffractometer with Cu Kα radiation (λ = 1.54178 Å) under ambient conditions. TGA was carried out on a Seiko Instruments (Tokyo, Japan) TG/DTA 6200 (EXSTER6000) at a heating rate of 10 °C min^{-1} under N_2. The magnetic properties of the composites were analyzed on a Riken Denshi (Tokyo, Japan) BHV-30 series vibrating sample magnetometer under ambient conditions. The optical absorbance was measured on an AS ONE (Osaka, Japan) ASV11D UV−visible spectrophotometer. Water was deionized on a Nomura Micro Science (Kanagawa, Japan) MINIPURE TW-300RU.

4.3. Synthesis of NICS. NICS was synthesized by modifying the reported method for CS functionalization.[62] CS (1.0 g, 6.1 mmol glucosamine unit) was dissolved in 200 mL of acetate buffer (pH 5.5) with magnetic stirring overnight. IAn (0.34 g, 3.0 mmol) dissolved in 10 mL of methanol was added dropwise to the CS solution for 30 min. The reaction mixture was magnetically stirred at room temperature for 12 h and neutralized with 10 M NaOH aq. The neutralized mixture was then added dropwise to an excess amount of acetone to precipitate NICS, and it was separated by centrifugation. Crude NICS was redispersed in DDW and reprecipitated in acetone. Purified NICS was dried in a vacuum desiccator at ambient temperature and obtained as a colorless flake with 85% yield. ^{1}H NMR (400 MHz, D_2O, 90 °C, δ in ppm): 2.5−2.6 (3H, $-COCH_3$), 3.10−3.30 (2H, $-CH_2-COO^-$), 3.7−3.9 (1H, $>C_2H-$), 4.0−4.4 (5H, $>C_3H-$, $>C_4H-$, $>C_5H-$, and $-C_6H_2-$), 4.9−5.0 (1H, $>C_1H$), 6.0−6.1 (1H, $>C{=}CH^b$), and 6.4−6.5 (1H, $>C{=}CH^{b'}$). FTIR (cm^{-1}): 571, 1067, 1382, 1559, 1652, 2882, 2921, 3088, and 3385. XRD (2θ in deg): 8.5 and 20.

4.4. Preparation of Fe_3O_4-NICS-EGDE Nanocomposite Particles. NICS (100 mg) was dispersed in a flask containing 180 mL of DDW by magnetic stirring. $FeCl_3·6H_2O$ (270 mg, 1.00 mmol) and $FeSO_4·7H_2O$ (139 mg, 0.50 mmol) were dissolved in 10 mL of DDW in an N_2 atmosphere. Both mixtures were added to a two-necked flask, and the flask was placed in a thermostat oil bath maintained at 80 °C. The final light brown mixture was homogenized by magnetic stirring while bubbling N_2. Then, 5.0 mL of aqueous ammonia solution (28%) was added at once, and the color of the mixture instantly turned from light brown to dark black. After 30 min of reaction, EGDE (25 mg, 1.0 mmol) dispersed in 5.0 mL of DDW was added dropwise to the mixture, and the reaction was continued for 30 min. The mixture was cooled to room temperature after the reaction. The resulting Fe_3O_4-NICS-EGDE nanocomposite particles were collected using a magnet and extensively washed with DDW until the pH value of the supernatant became neutral. The washed Fe_3O_4-NICS-EGDE nanocomposite particles were dried in a vacuum desiccator at ambient temperature for 24 h and kept in a refrigerator for further use.

4.5. Functionalization of Fe_3O_4-NICS-EGDE Nanocomposite Particles with EA. Fe_3O_4-NICS-EGDE nanocomposite particles (250 mg, 0.303 mmol glucosamine unit) were dispersed in 200 mL of DDW. EA (500 mg, 0.151 mmol) diluted in 50 mL of DDW was added dropwise to the dispersion for 30 min. The dispersion was magnetically stirred for 24 h at room temperature in the dark. The reaction mixture was then slowly added to a 1:1 (v/v) mixture of water and methanol to precipitate the product. The precipitate was collected by a magnet and repeatedly rinsed with DDW. The washed product was dried in a vacuum desiccator for 24 h in the dark and stored in a refrigerator.

4.6. Model Reaction of NICS and EA. The reaction of NICS (0.303 mmol glucosamine unit) and EA (0.151 mmol) was conducted under the identical conditions following the procedure described for the functionalization of the Fe_3O_4-NICS-EGDE nanocomposite with EA (Scheme 2). After the reaction, the reaction mixture was added dropwise to an excess amount of acetone to precipitate the product, and the precipitate was separated by filtration. The crude product was dissolved in DDW, and the solution was poured into an excess amount of acetone. The reprecipitated product (yield 80%) was dried in a vacuum desiccator for 48 h. ^{1}H NMR (400 MHz, D_2O, δ in ppm): 1.80−1.90 (3H, $-COCH_3$), 2.40−2.70 (3H, $-OOC-CH_2-C\underline{H}<$), 2.94 (2H, $-NH-CH_2-$), 3.05−3.12 (2H, $-OOC-CH_2-C{=}C<$), 3.30 (2H, $>CH-CH_2-NH-$), 3.40−3.50 (1H, $>CH-$), 3.55−3.65 (2H, $-CH_2-OH$), 4.2−4.55 (5H, $>C_3H-$, $>C_4H-$, $>C_5H-$ and $-C_6H_2-$), 4.90 (1H, $>C_1H-$), 5.25−5.35 (1H, $>C{=}CH^a-$), and 5.7−5.8 (1H, $>C{=}CH^b-$).

4.7. Buffer Capacity Analysis. The buffering capacities of the nanocomposites were evaluated by acid−base titration. The nanocomposite particles (1.0 mg mL^{-1}) were dispersed in 20 mL of NaCl aq. (0.150 M) buffer. After adding 0.1 mL of NaOH aq. (1.0 M) to the mixture, the basic dispersion was titrated with 0.1 M HCl aq. solution. The pH values were recorded by a HORIBA (Kyoto, Japan) 9615-10D pH meter.

4.8. Hemocompatibility Study. Hemolysis activities of the Fe_3O_4-NICS-EGDE-EA nanocomposite particles were assayed with modifications to the reported method.[54] Sheep whole blood (40 mL) was centrifuged at 3500 rpm for 5 min. RBCs were separated by careful decantation of supernatant plasma and then washed with physiological buffer (150 mM

DOI: 10.1021/acsomega.7b01918
ACS Omega 2018, 3, 961−972

NaCl aq.) three times. The washed RBCs were redispersed in physiological buffer (40 mL). The charge-conversional Fe_3O_4-NICS-EGDE-EA nanocomposite particles dispersed in physiological buffer was mixed with the RBC suspension. The final concentrations of the nanocomposite in the dispersion were adjusted to 100, 200, 400, and 600 μg mL^{-1}. The pH of the dispersions was adjusted to the corresponding values (5.0−7.4) using 0.01 N HCl aq. solution. Triton X-100 (1% aq. solution) and physiological buffer were added to the RBC suspensions to prepare the positive (100% lysis) and negative (0% lysis) control samples, respectively. All of the samples were incubated at 37 °C for 1, 3, and 5 h. The samples were gently shaken once every 20 min for resuspension. After incubation, the RBCs were separated by centrifugation (10 000 rpm, 5 min) and the supernatant solutions were incubated for 30 min at room temperature to oxidize hemoglobin. The absorbance of oxyhemoglobin was assessed by optical absorption at 540 nm. The hemolysis (%) of RBCs was calculated using the following equation

$$\%\text{hemolysis} = \{(\text{Abs}_{\text{sample}} - \text{Abs}_{\text{negative control}}) / (\text{Abs}_{\text{positive control}} - \text{Abs}_{\text{negative control}})\} \times 100$$

For MW-induced magnetically triggered hemolysis experiments, the samples were made following the aforementioned procedures. Before centrifugation, the samples were exposed to MW radiation (2.45 GHz) for 30 s with an output power of 200 W, and the temperatures of the dispersions were recorded. All experiments were performed in duplicate, and the resulting data were shown as average values.

4.9. Studies of RBC Morphology. The morphology of RBCs was observed using a light microscope. In brief, the washed RBCs were added to a physiological buffer containing the charge-conversional Fe_3O_4-NICS-EGDE-EA nanocomposite particles at 600 μg mL^{-1}, and the pH value was adjusted to 5.5 using 0.01 M HCl aq. The resulting dispersion was incubated at 37 °C for 5 h and mildly shaken once every 20 min. After incubation, the dispersion was treated with a magnet to remove free nanocomposite particles. Then, the RBCs were separated by centrifugation, further washed, and redispersed in physiological buffer. A control sample was also made without adding the nanocomposite. The washed RBC suspension (10 μL) was placed on a glass slide and covered with a coverslip glass. The resulting specimens were observed with an Olympus (Tokyo, Japan) CKX53 microscope, and the color pictures were captured using a Visualix Pro2 (Kobe, Japan) camera. All images were taken at the magnification of 20×.

4.10. Magnetic Heating under MW Irradiation (Typical Procedure). The MW irradiation experiments were conducted in a Yamazen (Osaka, Japan) MW-Y205 MW oven operated at 2.45 GHz with a radiation output power of 200 W. A 200 mL Erlenmeyer flask containing 100 mL of a colloidal dispersion of 100 μg mL^{-1} of the charge-conversional Fe_3O_4-NICS-EGDE-EA nanocomposite particles and another 200 mL Erlenmeyer flask containing 100 mL of water were placed together in the oven. The second flask was added as a dummy load to absorb excessive MW radiation power. The dispersions were exposed to sequential 0.25−3.0 min of MW irradiation, and the temperature was subsequently measured with an A & D (Tokyo, Japan) AD-5612WP dual-mode infrared thermometer. The sample mixtures were shaken gently before each measurement to attain bulk temperature. Temperature equilibration and the measurements were conducted within 10 s. Each heating experiment was conducted in 5 min intervals to attain homogeneous exposure of MW radiation to samples. All experiments were performed in triplicates, and the results are shown with corresponding error bars.

■ ASSOCIATED CONTENT

Supporting Information

The Supporting Information is available free of charge on the ACS Publications website at DOI: 10.1021/acsomega.7b01918.

Characterization of NICS; ^{1}H NMR spectrum of NICS-EA; EDX spectra; XRD analysis; unit cell characterization of the charge-conversional Fe_3O_4-NICS-EGDE-EA nanocomposite particles; TGA analysis; time-dependent hemolysis; hemolytic activities of Fe_3O_4-NICS-EGDE nanocomposite particles; light microscopic observation of the hemolysis; membranolysis of sheep RBCs at pHs 6.8 and 6.5 (PDF)

■ AUTHOR INFORMATION

Corresponding Author

*E-mail: ochiai@yz.yamagata-u.ac.jp.

ORCID

Bungo Ochiai: 0000-0002-4376-8875

Notes

The authors declare no competing financial interest.

■ ACKNOWLEDGMENTS

The authors thank Dr. Kunihiro Koike of Yamagata University for his kind assistance in measuring magnetism. M.A.R. is grateful to the Ministry of Education, Culture, Sports, and Technology, Japan, for providing Monbukagakusho (MEXT) scholarship. The authors extend their sincere thanks to Editage (www.editage.jp) for English language editing.

■ REFERENCES

(1) Lin, J.; Li, Y.; Li, Y.; Wu, H.; Yu, F.; Zhou, S.; Xie, L.; Luo, F.; Lin, C.; Hou, Z. Drug/Dye-Loaded, Multifunctional PEG-Chitosan-IronOxide Nanocomposites for Methotraxate Synergistically Self-Targeted Cancer Therapy and Dual Model Imaging. *ACS Appl. Mater. Interfaces* **2015**, *7*, 11908−11920.

(2) Kamat, M.; El-Boubbou, K.; David, C. Z.; Lansdell, T.; Lu, X.; Li, W.; Huang, X. Hyaluronic Acid Immobilized Magnetic Nanoparticles for Active Targeting and Imaging of Macrophages. *Bioconjugate Chem.* **2010**, *21*, 2128−2135.

(3) Saadat, R.; Renz, F. Simultaneous Cancer Control and Diagnosis with Magnetic Nanohybrid Materials. *Beilstein J. Nanotechnol.* **2016**, *7*, 121−125.

(4) Cheng, D.; Li, X.; Zhang, C.; Tan, H.; Wang, C.; Pang, L.; Shi, H. Detection of Vulnerable Atherosclerosis Plaques with a Dual-Modal Single-Photon-Emission Computed Tomography/Magnetic Resonance Imaging Probe Targeting Apoptotic Macrophages. *ACS Appl. Mater. Interfaces* **2015**, *7*, 2847−2855.

(5) Chen, T.-J.; Cheng, T. H.; Chen, C. Y.; Hsu, S.; Cheng, T. L.; Liu, G. C.; Wang, Y. M. Targeted Herceptin-Dextran Iron Oxide Nanoparticles for Noninvasive Imaging of HER2/neu Receptors Using MRI. *J. Biol. Inorg. Chem.* **2009**, *14*, 253−260.

(6) Yang, L.; Mao, H.; Wang, Y. A.; Cao, Z.; Peng, X.; Wang, X.; Duan, H.; Ni, C.; Yuan, Q.; Adams, G.; Smith, M. Q.; Wood, W. C.; Gao, X.; Nie, S. Single Chain Epidermal Growth Factor Receptor Antibody Conjugated Nanoparticles for In Vivo Tumor Targeting and Imaging. *Small* **2009**, *5*, 235−243.

(7) Yu, M. K.; Park, J.; Jon, S. Targeting Strategies for Multifunctional Nanoparticles in Cancer Imaging and Therapy. *Theranostics* **2012**, *2*, 3−44.

DOI: 10.1021/acsomega.7b01918
ACS Omega 2018, 3, 961−972

(8) Lim, E. K.; Sajomsang, W.; Choi, Y.; Jang, E.; Lee, H.; Kang, B.; Kim, E.; Haam, S.; Suh, J. S.; Chung, S. J.; Huh, Y. M. Chitosan-Based Intelligent Theragnosis Nanocomposites Enable pH-Sensitive Drug Release with MR-Guided Imaging for Cancer Therapy. *Nanoscale Res. Lett.* **2013**, *8*, 467−478.
(9) Namiki, Y.; Namiki, T.; Yoshida, H.; Ishii, Y.; Tsubota, A.; Koido, S.; Nariai, K.; Mitsunaga, M.; Yanagisawa, S.; Kashiwagi, H.; Mabashi, Y.; Yumoto, Y.; Hoshina, S.; Fujise, K.; Tada, N. A Novel Magnetic Crystal-Lipid Nanostructure for Magnetically Guided *In Vivo* Gene Delivery. *Nat. Nanotechnol.* **2009**, *4*, 598−606.
(10) Liu, J.; Wei, T.; Zhao, J.; Huang, Y.; Deng, H.; Kumar, A.; Wang, C.; Liang, Z.; Ma, X.; Liang, X. Multifunctional Aptamer-Based Nanoparticles for Targeted Drug Delivery to Circumvent Cancer Resistance. *Biomaterials* **2016**, *91*, 44−56.
(11) Faraji, A. H.; Wipf, P. Nanoparticles in Cellular Drug Delivery. *Bioorg. Med. Chem.* **2009**, *17*, 2950−2962.
(12) Conde, J.; Dias, J. T.; Grazu, V.; Moros, M.; Baptista, P. V.; de la Fuente, J. M. Revisiting 30 Years of Biofunctionalization and Surface Chemistry of Inorganic Nanoparticles for Nanomedicine. *Front. Chem.* **2014**, *2*, 48.
(13) Hardiansyah, A.; Yang, M. C.; Liu, T. Y.; Kuo, C. Y.; Huang, L. Y.; Chan, T. Y. Hydrophobic Drug-Loaded PEGylated Magnetic Liposomes for Drug-Controlled Release. *Nanoscale Res. Lett.* **2017**, *12*, 355−365.
(14) Mishra, S.; Webster, P.; Davis, M. E. PEGylation Significantly Affects Cellular Uptake and Intracellular Trafficking of Non-Viral Gene Delivery Particles. *Eur. J. Cell Biol.* **2004**, *83*, 97−111.
(15) Sawant, R. R.; Torchilin, V. P. Liposomes as 'Smart' Pharmaceutical Nanocarriers. *Soft Matter* **2010**, *6*, 4026−4044.
(16) Hatakeyama, H.; Akita, H.; Harashima, H. A Multifunctional Envelope Type Nano Device (MEND) for Gene Delivery to Tumours Based on the EPR Effect: A Strategy for Overcoming the PEG Dilemma. *Adv. Drug Delivery Rev.* **2011**, *63*, 152−160.
(17) Sato, Y.; Hatakeyama, H.; Sakurai, Y.; Hyodo, M.; Akita, H.; Harashima, H. A pH-Sensitive Cationic Lipid Facilitates the Delivery of Liposomal siRNA and Gene Silencing Activity *In Vitro* and *In Vivo*. *J. Controlled Release* **2012**, *163*, 267−276.
(18) Smith, B.; Lyakhov, I.; Loomis, K.; Needle, D.; Baxa, U.; Yavlovich, A.; Capala, J.; Blumenthal, R.; Puri, A. Hyperthermia-Triggered Intracellular Delivery of Anticancer Agent to $HER2^+$ Cells by HER2-Specific Affibody (ZHER2-GS-Cys)-Conjugated Thermosensitive Liposomes ($HER2^+$ Affisomes). *J. Controlled Release* **2011**, *153*, 187−194.
(19) Sundaresan, V.; Menon, J. U.; Rahimi, M.; Nguyen, K. T.; Wadajkar, A. S. Dual-Responsive Polymer-Coated Iron Oxide Nanoparticles for Drug Delivery and Imaging Applications. *Int. J. Pharm.* **2014**, *466*, 1−7.
(20) Ta, T.; Bartolak-Suki, E.; Park, E. J.; Karrobi, K.; McDannold, N. J.; Porter, T. M. Localized Delivery of Doxorubicin *In Vivo* from Polymer-Modified Thermosensitive Liposomes with MR-Guided Focused Ultrasound-Mediated Heating. *J. Controlled Release* **2014**, *194*, 71−81.
(21) Alupei, L.; Peptu, A. C.; Lungan, A. M.; Desbrieres, J.; Chiscan, O.; Radji, S.; Popa, M. New Hybrid Magnetic Nanoparticles Based on Chitosan-Maltose Derivative for Antitumor Drug Delivery. *Int. J. Biol. Macromol.* **2016**, *92*, 561−572.
(22) Lungu, I. I.; Rădulescu, M.; Mogoşanu, G. D.; Grumezescu, A. M. pH Sensitive Core-Shell Magnetic Nanoparticles for Targeted Drug Delivery in Cancer Therapy. *Rom. J. Morphol. Embryol.* **2016**, *57*, 23−32.
(23) Suarato, G.; Li, W.; Meng, Y. Role of pH-Responsiveness in the Design of Chitosan-Based Cancer Nanotherapeutics: A Review. *Biointerphases* **2016**, *11*, 04B201−04B217.
(24) Jaiswal, M. K.; Pradhan, A.; Banerjee, R.; Bahadur, D. Dual pH and Temperature Stimuli-Responsive Magnetic Nanohydrogels for Thermo-Chemotherapy. *J. Nanosci. Nanotechnol.* **2014**, *14*, 4082−4089.
(25) Hervault, A.; Dunn, A. E.; Lim, M.; Boyer, C.; Mott, D.; Maenosono, S.; Thanh, N. T. K. Doxorubicin Loaded Dual pH- and Thermo-Responsive Magnetic Nanocarrier for Combined Magnetic Hyperthermia and Targeted Controlled Drug Delivery Applications. *Nanoscale* **2016**, *8*, 12152−12161.
(26) Barick, K. C.; Singh, S.; Jadhav, N. V.; Bahadur, D.; Pandey, B. N.; Hassan, P. A. pH-Responsive Peptide Mimic Shell Cross-Linked Magnetic Nanocarriers for Combination Therapy. *Adv. Funct. Mater.* **2012**, *22*, 4975−4984.
(27) Zhang, H.; Xue, Y.; Huang, J.; Xia, X.; Song, M.; Wen, K.; Zhang, X.; Luo, X.; Cai, N.; Long, S.; Yu, F. Tailor-Made Magnetic Nanocarriers with pH-Induced Charge Reversal and pH-Responsiveness to Guide Subcellular Release of Doxorubicin. *J. Mater. Sci.* **2015**, *50*, 2429−2442.
(28) Huang, X.; Meng, X.; Tang, F.; Li, L.; Chen, D.; Liu, H.; Zhang, Y.; Ren, J. Mesoporous Magnetic Hollow Nanoparticles-Protein Carriers for Lysosome Escaping and Cytosolic Delivery. *Nanotechnology* **2008**, *19*, No. 445101.
(29) Wu, J.; Jiang, W.; Shen, Y.; Jiang, W.; Tian, R. Synthesis and Characterization of Mesoporous Magnetic Nanocomposites Wrapped with Chitosan Gatekeepers for pH-Sensitive Controlled Release of Doxorubicin. *Mater. Sci. Eng., C* **2017**, *70*, 132−140.
(30) Pramanik, A.; Jones, S.; Pedraza, F.; Vangara, A.; Sweet, C.; Williams, M. S.; Ruppa-Kasani, V.; Risher, S. E.; Sardar, D.; Ray, P. C. Fluorescent, Magnetic Multifunctional Carbon Dots for Selective Separation, Identification, and Eradication of Drug-Resistant Superbugs. *ACS Omega* **2017**, *2*, 554−562.
(31) Giustini, A. J.; Petryk, A. A.; Cassim, S. M.; Tate, J. A.; Baker, I.; Hoopes, P. J. Magnetic Nanoparticle Hyperthermia in Cancer Treatment. *Nano Life* **2010**, *1*, 17−32.
(32) Moroz, P.; Jones, S. K.; Gray, B. N. Magnetically Mediated Hyperthermia: Current Status and Future Directions. *Int. J. Hyperthermia* **2002**, *18*, 267−284.
(33) Blanco-Andujar, C.; Ortega, D.; Southern, P.; Pankhurst, Q. A.; Thanh, N. T. K. High Performance Multi-Core Iron Oxide Nanoparticles for Magnetic Hyperthermia: Microwave Synthesis, and the Role of Core-to-Core Interactions. *Nanoscale* **2015**, *7*, 1768−1775.
(34) van der Zee, J. Heating the Patient: A Promising Approach? *Ann. Oncol.* **2002**, *13*, 1173−1184.
(35) Tasci, T. O.; Vargel, I.; Arat, A.; Guzel, E.; Korkusuz, P.; Atalar, E. Focused RF Hyperthermia Using Magnetic Fluids. *Med. Phys.* **2009**, *36*, 1906−1912.
(36) Tseng, H. Y.; Lee, G. B.; Lee, C. Y.; Shih, Y. H.; Lin, X. Z. Localised Heating of Tumours Utilising Injectable Magnetic Nanoparticles for Hyperthermia Cancer Therapy. *IET Nanobiotechnol.* **2009**, *3*, 46−54.
(37) Jung, H. Interaction of Thermotolerance and Thermosensitization Induced in CHO Cells by Combined Hyperthermic Treatments at 40 and 43 °C. *Radiat. Res.* **1982**, *91*, 433−446.
(38) Zhang, J.; Dewilde, A. H.; Chinn, P.; Foreman, A.; Barry, S.; Kanne, D.; Braunhut, S. J. Herceptin-Directed Nanoparticles Activated by an Alternating Magnetic Field Selectively Kill HER-2 Positive Human Breast Cells *In Vitro* via Hyperthermia. *Int. J. Hyperthermia* **2011**, *27*, 682−697.
(39) Kikumori, T.; Kobayashi, T.; Sawaki, M.; Imai, T. Anti-Cancer Effect of Hyperthermia on Breast Cancer by Magnetite Nanoparticle-Loaded Anti-HER2 Immunoliposomes. *Breast Cancer Res. Treat.* **2009**, *113*, 435−441.
(40) Thiesen, B.; Jordan, A. Clinical Applications of Magnetic Nanoparticles for Hyperthermia. *Int. J. Hyperthermia* **2008**, *24*, 467−474.
(41) Maier-Hauff, K.; Ulrich, F.; Nestler, D.; Niehoff, H.; Wust, P.; Thiesen, B.; Orawa, H.; Budach, V.; Jordan, A. Efficacy and Safety of Intratumoral Thermotherapy Using Magnetic Iron-Oxide Nanoparticles Combined with External Beam Radiotherapy on Patients with Recurrent Glioblastoma Multiforme. *J. Neuro-Oncol.* **2011**, *103*, 317−324.
(42) Edward, C.; Halperin, M. D.; Luther, W.; Brady, M. D.; Carlos, A.; Perez, M. D.; David, E.; Wazer, M. D. *Perez and Brady's Principles and Practice of Radiation Oncology*; Wolters Kluwer Health/Lippincott Williams & Wilkins: Philadelphia, 2008; pp 637−644.

DOI: 10.1021/acsomega.7b01918
ACS Omega 2018, 3, 961−972

(43) Adi, V.; Earn, A. B.; Menachem, M.; Dror, M.; Yossef, D.; Zeev, Z.; Rachela, P. Targeted Magnetic Nanoparticles for Mechanical Lysis of Tumor Cells by Low-Amplitude Alternating Magnetic Field. *Materials* **2016**, *9*, 943−954.
(44) Carrey, J.; Connord, V.; Respaud, M. Ultrasound Generation and High-Frequency Motion of Magnetic Nanoparticles in an Alternating Magnetic Field: Toward Intracellular Ultrasound Therapy? *Appl. Phys. Lett.* **2013**, *102*, 232404.
(45) Domenech, M.; Marrero-Berrios, I.; Torres-Lugo, M.; Rinaldi, C. Lysosomal Membrane Permeabilization by Targeted Magnetic Nanoparticles in Alternating Magnetic Fields. *ACS Nano* **2013**, *7*, 5091−5101.
(46) Iovino, N.; Bohorquez, A.; Rinaldi, C. Magnetic Nanoparticle Targeting of Lysosomes: A Viable Method of Overcoming Tumor Resistance? *Nanomedicine* **2014**, *9*, 937−939.
(47) Allen, C.; Dos, S. N.; Gallagher, R.; Chiu, G. N.; Shu, Y.; Li, W. M.; Johnstone, S. A.; Janoff, A. S.; Mayer, L. D.; Webb, M. S.; Bally, M. B. Controlling the Physical Behavior and Biological Performance of Liposome Formulations Through Use of Surface Grafted Poly-(Ethylene Glycol). *Biosci. Rep.* **2002**, *22*, 225−250.
(48) Aiping, Z.; Tian, C.; Lanhua, Y.; Hao, W.; Ping, L. Synthesis and Characterization of *N*-Succinyl-Chitosan and its Self-Assembly of Nanospheres. *Carbohydr. Polym.* **2006**, *66*, 274−279.
(49) Waldron, R. D. Infrared Spectra of Ferrites. *Phys. Rev.* **1955**, *99*, 1727−1735.
(50) Cornel, R. M.; Schwertmann, U. *The Iron Oxides: Structure, Properties, Reactions, Occurrences and Uses*; Wiley-VCH: Weinheim, 2003.
(51) Ahmad, H.; Rahman, M. A.; Miah, M. A. J.; Tauer, K. Magnetic and Temperature-Sensitive Composite Polymer Particles and Adsorption Behavior of Emulsifiers and Trypsin. *Macromol. Res.* **2008**, *16*, 637−643.
(52) Dolatkhah, A.; Wilson, L. D. Magnetite/Polymer Brush Nanocomposites with Switchable Uptake Behavior Toward Methylene Blue. *ACS Appl. Mater. Interfaces* **2016**, *8*, 5595−5607.
(53) Brian, C. S. The Infrared Spectroscopy of Alkenes. *Spectroscopy* **2016**, *31*, 28−34.
(54) Rahman, M. A.; Ochiai, B. Fabrication and Hemocompatibility of Carboxy-Chitosan Stabilized Magnetite Nanoparticles. *Microsyst. Technol.* **2017**, 1−13.
(55) Wu, J.; Yang, J. Superlong Salicylideneaniline Semiconductor Nanobelts Prepared by a Magnetic Nanoparticle-Assisted Self-Assembly Process for Luminescence Thermochromism. *ACS Omega* **2017**, *2*, 2264−2272.
(56) Andrzejewski, B.; Bednarskia, W.; Kaźmierczaka, M.; Pogorzelec-Glasera, K.; Hilczera, B.; Jurga, S.; Matczaka, M.; Łęskac, B.; Pankiewiczc, R.; Kępińskid, L.; et al. Magnetization Enhancement in Magnetite Nanoparticles Capped with Alginic Acid. *Composites, Part B* **2014**, *64*, 147−154.
(57) Singhal, J. P.; Ray, A. R. Synthesis of Blood Compatible Polyamide Block Copolymers. *Biomaterials* **2002**, *23*, 1139−1145.
(58) Tokumasu, F.; Ostera, G. R.; Amaratunga, C.; Fairhurst, R. M. Modifications in Erythrocyte Membrane Zeta Potential by Plasmodium Falciparum Infection. *Exp. Parasitol.* **2012**, *131*, 245−251.
(59) Ojugo, A. S. E.; Mcsheehy, P. M. J.; Mcintyre, D. J. O.; Mccoy, C.; Stubbs, M.; Leach, M. O.; Judson, I. R.; Griffiths, J. R. Measurement of the Extracellular pH of Solid Tumours in Mice by Magnetic Resonance Spectroscopy: A Comparison of Exogenous ^{19}F and ^{31}P probes. *NMR Biomed.* **1999**, *12*, 495−504.
(60) Tannock, I. F.; Rotin, D. Acid pH in Tumors and Its potentials for Therapeutic Exploitation. *Cancer Res.* **1989**, *49*, 4373−4384.
(61) Rotin, D.; Wan, P.; Grinstein, S.; Tannock, I. Cytotoxicity of Compounds that Interfere with the Regulation of Intracellular pH: A Potential New Class of Anticancer Drugs. *Cancer Res.* **1987**, *47*, 1497−1504.
(62) Sashiwa, H.; Shigemasa, Y. Chemical Modification of Chitin and Chitosan 2: Preparation and Water Soluble Property of *N*-Acylated or *N*-Alkylated Partially Deacetylated Chitins. *Carbohydr. Polym.* **1999**, *39*, 127−138.

DOI: 10.1021/acsomega.7b01918
ACS Omega 2018, 3, 961−972